Investigation of the first and second aerosol indirect effects using data from the May 2003 Intensive Operational Period at the Southern Great Plains

Huan Guo,[1] Joyce E. Penner,[1] Michael Herzog,[2] and Shaocheng Xie[3]

[1] The Active Tracer High-Resolution Atmospheric Model is used to examine the aerosol indirect effect (AIE) for a spring continental stratus cloud on the basis of data collected during the 17 May 2003 Aerosol Intensive Operation Period (AIOP) at the Atmospheric Radiation Measurement (ARM) Program Southern Great Plains site. Model results for our base case, which uses observed aerosol concentrations, agree reasonably well with the available observations, giving confidence that the basic model is reasonable. Sensitivity tests are performed to explore the response of the clouds to changes in the aerosol number concentration and surface fluxes. During the major part of the simulation, from 0630 through 1400 local standard time (LST), an increase in the aerosol number concentration (N_a) results in a decrease of the mean cloud droplet size and an increase of the cloud liquid water path (LWP) until aerosol number concentration levels reach 1200 cm^{-3}. Further increases in aerosol concentration do not increase the liquid water path because the depletion of cloud water by precipitation is negligible above this number concentration. After 1400 LST, the liquid water path decreases when aerosols increase as long as $N_a < 600$ cm^{-3} and remains unchanged for higher aerosol concentrations. The decrease of LWP is associated with the evaporative cooling below cloud base which leads to more condensation of water vapor, a result that is consistent with afternoon satellite observations of the response of continental clouds to increases in droplet concentrations. A sensitivity test with a stronger surface latent flux increases both the cloud geometrical thickness and cloud water content. On the other hand, a sensitivity test with a stronger surface sensible heat flux leads to a higher cloud base and a shallower and drier cloud. The response of the cloud geometrical thickness to changes in surface sensible heat flux dominates that of the cloud water content. The cloud fraction is also reduced at the end of the simulation time period. Because the surface heat fluxes will likely change when aerosol and droplet number concentrations change, these sensitivity tests show that a fully coupled simulation with a land surface model will be needed to fully assess the response of the cloud to changing aerosol concentrations. Nevertheless, since the thermodynamic boundary layer profiles do not change significantly when aerosol concentrations are changed, our results for changing aerosol concentrations are qualitatively correct.

1. Introduction

[2] Aerosol-cloud-radiation interactions are an integral and important part of the climate system. Unfortunately, their representation is far from precise in most state-of-the-art global climate models (GCMs) [*Haywood and Boucher*, 2000; *Lohmann and Feichter*, 2005]. The aerosol indirect effect (AIE) has been estimated to vary from 0.0 to −4.8 W m^{-2} [*Penner et al.*, 2001]. This high uncertainty has stimulated substantial research in recent years. This research has focused on the first AIE, on the second AIE, or on both.

[3] The first AIE, or "Twomey" effect, refers to the modification of the cloud droplet number concentration (N_d) by aerosols [*Twomey*, 1977] while keeping other macrophysical properties of the cloud constant. The first

[1]Department of Atmospheric, Oceanic and Space Sciences, University of Michigan, Ann Arbor, Michigan, USA.
[2]Geophysical Fluid Dynamics Laboratory, National Oceanic and Atmospheric Administration, Princeton, New Jersey, USA.
[3]Atmospheric Science Division, Lawrence Livermore National Laboratory, Livermore, California, USA.

AIE is widely supported by a variety of measurements, e.g., in situ airborne measurements and ground-based remote sensing [*Brenguier et al.*, 2000; *Penner et al.*, 2004]. The second AIE was first proposed by *Albrecht* [1989]. He showed that the suppression of precipitation by aerosols could increase cloud water content (or cloud liquid water path, LWP) and fractional cloud cover. However, the second AIE is often complicated by the meteorological background, cloud dynamics, turbulence, [*Ackerman et al.*, 2004; *Lu and Seinfeld*, 2005], and even surface processes [*Jiang and Feingold*, 2006]. Therefore the second AIE is extremely difficult to quantify [*Penner et al.*, 2001].

[4] The study of the AIE in maritime clouds has attracted considerable attention in recent years [*Jiang et al.*, 2002; *Ackerman et al.*, 2003, 2004; *Guo et al.*, 2007]. *Lu and Seinfeld* [2005] examined an ensemble of 98 three-dimensional large eddy simulations of marine stratocumulus clouds, and showed that the LWP responded primarily to the large-scale subsidence and sea surface temperature. The LWP tended to be positively correlated with N_a when there was heavy surface precipitation; otherwise it was not.

[5] Are these results also applicable to continental clouds? It is surprising that continental clouds have not received the same scrutiny as marine clouds, even though most GCMs suggest that the total AIE is at least as large over land as over oceans [*Lohmann and Feichter*, 2005]. The continental boundary layer differs significantly from the marine boundary layer because it undergoes a significant diurnal cycle as do the land surface sensible and latent heat fluxes [*Stull*, 1988; *Garstang and Fitzjarrald*, 1999; *Medeiros et al.*, 2005].

[6] *Han et al.* [2002] used satellite data to examine the global cloud liquid water path sensitivity (δ) to cloud droplet number concentration during the daytime, specifically during local afternoon (Note: δ is defined as the ratio of the change of cloud LWP to the change of column-integrated cloud droplet number concentration (N_c), that is, $\delta = \frac{\Delta LWP}{\Delta N_c}$). They analyzed δ over oceans and over land. According to their analysis, for marine clouds there are areas with both large positive and large negative δ. However, for most continental clouds, δ is neutral or slightly negative. This may mean that an increase of N_a, and therefore N_c, does not necessarily result in an increase of cloud LWP, which could imply a negligible or even positive second AIE [*Albrecht*, 1989].

[7] To advance our scientific understanding of aerosol-cloud-radiation interactions, the U.S. DOE (Department of Energy) ARM program conducted an Aerosol Intensive Operation Period (AIOP) at its Southern Great Plains (SGP) site in May 2003 [*Ferrare et al.*, 2006]. During this AIOP, measurements of the cloud condensation nucleus concentration (CCN) as a function of supersaturation were taken to relate CCN concentration to aerosol composition and size distribution. Airborne and remote-sensing techniques provided extensive measurements of the droplet effective radius, cloud morphology, and cloud optical depth. These data offer a good opportunity to study the role of aerosols in continental clouds.

[8] In this study, we use a cloud resolving model (CRM), i.e., the Active Tracer High-Resolution Atmospheric Model (ATHAM), to explore the effects of aerosols on the cloud droplet effective radius (R_e) and on the cloud LWP. The case we examine is a stratus cloud that occurred on 17 May 2003.

We first evaluate the model's performance by comparing our base case simulation to observations. Then sensitivity tests are examined to investigate both the AIE and the impact of the surface fluxes on the cloud development.

[9] The paper is organized as follows: Section 2 describes ATHAM and the simulation setup. Section 3 discusses results from the base case and compares them with observations. Section 4 presents a series of sensitivity tests. Section 5 discusses and summarizes our results.

2. Model Description and Simulation Setup

2.1. Model Description

2.1.1. Dynamic Framework

[10] ATHAM is a nonhydrostatic, fully compressible atmospheric model that solves the Navier-Stokes equations, and is formulated with a finite difference and a combined line relaxation successive overrelaxation integration scheme [*Oberhuber et al.*, 1998; *Herzog et al.*, 1998, 2003; *Textor et al.*, 2003; *Guo et al.*, 2004, 2005]. The model predicts momentum, potential temperature, pressure, turbulent kinetic energy (TKE), turbulent length scale, and tracers, e.g., specific humidity and cloud water content. The model solves the momentum and tracer equations in the flux form for better conservation properties. As is customary for CRMs, we applied a periodic lateral boundary condition. At the lower boundary, we assume a material surface, across which surface sensible heat and moisture fluxes pass. The model top is a rigid lid. At the upper part of the numerical domain (upper 20%), a sponge layer is applied to minimize the spurious reflection of upward propagating gravity waves.

2.1.2. Turbulence Scheme (Subgrid-Scale Parameterization)

[11] The current turbulence parameterization (or subgrid parameterization) in ATHAM adopts a 1.5-order closure scheme [*Herzog et al.*, 2003]. Rather than assuming local isotropy, this turbulence parameterization differentiates between horizontal and vertical turbulent mixing to enable it to describe the turbulent vertical transport more accurately. The horizontal and vertical turbulent diffusion coefficients are obtained from three coupled differential equations for the horizontal TKE, the vertical TKE, and the turbulent length scale. Compared to a fully second-order closure model, in which the computational effort is more than doubled to predict the second moments of the turbulence terms, the current turbulence scheme only solves one additional vertical TKE equation. Therefore the computational efficiency remains similar to the classical 1.5-order turbulence scheme but contains one of the main features of the second-order turbulence schemes.

2.1.3. Cloud Microphysics

[12] The cloud microphysical parameterization in ATHAM, follows a bulk scheme; that is, it explicitly predicts the bulk characteristics of a given water substance. For example, cloud liquid water mixing ratio (q_c) is calculated (in flux form) from

$$\frac{\partial \rho q_c}{\partial t} = \nabla \bullet \vec{u} \rho q_c + \nabla \bullet K \nabla \rho q_c + Q_{cond.} - Q_{evap.} - Q_{auto.} - Q_{accr.}, \tag{1}$$

where ρ is the air density, $\vec{u}$ is the wind velocity vector, K is the turbulent exchange coefficient, and $Q_{cond.}$, $Q_{evap.}$, $Q_{auto.}$, and $Q_{accr.}$ refer to the rates of condensation, evaporation, autoconversion, and accretion, respectively [*Oberhuber et al.*, 1998; *Herzog et al.*, 1998]. We have adopted Kessler's bulk scheme except for the autoconversion and accretion processes [*Kessler*, 1969, *Herzog et al.*, 1998]. For the autoconversion process, *Liu and Daum*'s [2004] 6th moment autoconversion parameterization is employed. In this parameterization, the autoconversion rate (Q_{auto}) depends on the cloud water, droplet concentration, and droplet dispersion:

$$Q_{auto.} = C_6(\rho q_c)^3 N_d^{-1} H(R_6 - R_{6r}), \quad (2)$$

where C_6 is a parameter that depends on the droplet dispersion, and $H(R_6 - R_{6r})$ is the Heaviside function which is used to establish the threshold for autoconversion which occurs only when the 6th moment of the droplet size R_6 exceeds a critical value R_{6r} (10 μm here). In addition, *Beheng*'s [1994] accretion scheme is applied, which depends on both cloud water and rain water (q_r):

$$Q_{accr.} = C_{accr.}(\rho q_c)(\rho q_r), \quad (3)$$

where $C_{accr.}$ is a parameter ($\sim$6.0 m^3 kg^{-1} s^{-1}).

[13] N_d is calculated following *Lohmann et al.* [1999]:

$$\frac{\partial N_d}{\partial t} = R(N_d) + Q_{nucl} - Q_{auto}(N_d) - Q_{self} - \frac{N_d}{\rho q_c}(Q_{accr} + Q_{evap}) \quad (4)$$

where $R(N_d)$ refers to the advective and turbulent transport of N_d, and Q_{nucl}, $Q_{auto}(N_d)$, and Q_{self} refer to the rates for nucleation, autoconversion, and self-collection of cloud droplets, respectively. During turbulent transport and mixing with dry air, N_d is assumed to be homogeneously mixed so that the total N_d is unaffected but the droplet size decreases during entrainment and/or mixing [*Grabowski*, 2006]. However, N_d is generally varies spatially and temporally because the advective transport and physical sources (sinks), e.g., nucleation, which depends on the updraft velocity, are inhomogeneous. The evaporation term ($\frac{N_d}{\rho q_c} Q_{evap}$) takes diabatic processes (e.g., solar heating or drying and large-scale advection) into account. Nevertheless, under most conditions, the contribution of the evaporation process to N_d is small.

[14] Nucleation is a critical process because it determines the initial concentration of cloud droplets. Here the nucleation parameterization developed by *Abdul-Razzak and Ghan* [2002] (hereafter AG2002) is used. AG2002's scheme is a physically based mechanistic aerosol activation scheme. The cloud droplet number concentration, N_d, is diagnosed from the updraft velocity, aerosol particle sectional size distribution and chemical composition (hygroscopicity). AG2002 showed that their parameterized results were within 10% of those from detailed numerical computations for both idealized and measured aerosol size distributions.

2.1.4. Radiative Transfer Module

[15] The shortwave radiative transfer module in ATHAM assumes a two-stream Delta-Eddington approximation to calculate the fluxes at the edges of the vertical layer. It has nine bands covering the ultraviolet and visible (UVV) region from 0.175 μm to 0.700 μm and three bands resolving water vapor absorption in the near infrared (IR) spectrum between 0.700 μm and 4.000 μm [*Grant et al.*, 1999]. The cloud optical depth (COD) depends on the LWP and droplet effective radius (R_e, the ratio between the third and the second moment of the droplet size distribution) via $COD = \frac{3LWP}{2R_e\rho_w}$, where ρ_w is the liquid water density and R_e is assumed to be linearly proportional to the droplet mean volume radius (R_v); that is, $R_e = \beta R_v$, where β is $\sim$1.143 for continental clouds [*Martin et al.*, 1994; *Lohmann et al.*, 1999]. R_v is determined by cloud water and N_d through $R_v = (\frac{3}{4}\frac{\rho q_c}{\pi N_d \rho_w})^{\frac{1}{3}}$. This linear relationship between R_e and R_v is generally valid for warm stratocumulus clouds when entrainment effects are small and precipitation is insignificant [*Martin et al.*, 1994]. We calculated the ratio of the 3rd and 2nd moments for the measured CAPS (Cloud-Aerosol-Precipitation-Spectrometer) size distribution and found $\beta = 1.215$ on average, in reasonable agreement with that suggested by *Martin et al.* [1994].

[16] The longwave radiation package includes parameterizations for the absorption of H_2O, O_3, CO_2, and for most of the minor trace species, e.g., N_2O, CH_4, CFC's, as well as warm and ice clouds [*Chou et al.*, 2001]. The longwave spectrum is divided into nine bands and one subband, which range from 0 cm^{-1} to 3000 cm^{-1}. Cloud radiative properties are fitted to high-spectral resolution extinction coefficients, single scattering albedos, and asymmetry factors by regression, and are parameterized as functions of cloud LWP and R_e [*Chou et al.*, 2001].

[17] The current version of ATHAM uses a broadband average surface albedo, which only depends on the underlying surface type, not on the solar wavelength and/or incidence angles. The surface albedo was fixed at 0.2 in this study on the basis of observations taken at the ARM site.

2.2. Simulation Setup

[18] The simulations described here used both the two-dimensional (2-D) and three-dimensional (3-D) versions of the model. The 2-D simulations used 416 × 151 grid points with a horizontal spacing of 125 m, and a stretched vertical spacing of 40 m below 2 km and 300 m near the model top (20 km). The 3-D simulations used 208 × 208 × 151 grid points with a horizontal spacing of 250 m and the same vertical spacing as in the 2-D simulations. We used a deep domain (20 km) to ensure that the model results are insensitive to the sponge treatment at the top of the model. This also ensures that the appropriate (shortwave/longwave) radiative heating and cooling rates are provided throughout the boundary layer. The domain height is generally deeper in this model than that used in other studies but is necessary to maintain numerical stability. The real atmosphere is even higher, of course, and the lower atmosphere is not entirely isolated from the upper atmosphere so this set up is not incorrect. Moreover, the vertical resolution that we use (40 m) is sufficient to resolve the boundary layer processes that we are interested in.

[19] The time step is 1.5 s. For computational efficiency, most simulations are 2-D unless explicitly stated (see notation using "3-D" in Table 1). Model results are archived

Table 1. Spatial and Temporal Averages of Droplet Concentrations ($\overline{N_d}$) and Droplet Radii ($\overline{R_e}$) From 0630 LST to 1630 LST Over Cloudy Cells and Spatial and Temporal Averages of Liquid Water Path ($\overline{LWP}$) and Drizzle Rate Below the Cloud Base ($\overline{Drizzle}$) From 0630 LST to 1400 LST (<1400 LST) and From 1400 LST to 1600 LST (>1400 LST) for the Cases With Increasing and Decreasing N_a[a]

Case	Framework	N_a, cm^{-3}	$\overline{N_d}$, cm^{-3}	$\overline{R_e}$, μm	$\overline{LWP}$, gm^{-2}, <1400 LST	$\overline{Drizzle}$, mm d^{-1}, <1400 LST	$\overline{LWP}$, gm^{-2}, >1400 LST	$\overline{Drizzle}$, mm d^{-1}, >1400 LST
N_a150	2-D	150	116	9.38	74.30	0.58	71.42	0.50
N_a150 (3-D)	3-D	150	114	9.22	73.82	0.58	71.08	0.50
N_a300	2-D	300	225	7.74	87.66	0.45	70.01	0.19
N_a600	2-D	600	455	6.46	109.20	0.21	67.61	0.02
N_a1200	2-D	1200	872	5.28	130.18	0.02	57.60	0.00
N_a1200 (3-D)	3-D	1200	851	5.24	129.36	0.02	56.85	0.00
N_a2400	2-D	2400	1384	4.51	130.46	0.00	57.63	0.00
N_a150_no_evap	2-D	150	109	9.27	61.61	0.64	42.84	0.40
N_a1200_no_evap	2-D	1200	847	5.11	122.04	0.04	55.98	0.01

[a]Cloud liquid water mixing ratio (q_c) > 0.001 g/kg and N_d > 5 cm^{-3}.

every 10 min. Important model fields (momentum, temperature, moisture, TKE, N_d, etc.) are saved as instantaneous fields. Some cloud microphysical (e.g., N_d) and macrophysical properties (e.g., LWP) are also saved as averages over each 10 min interval.

[20] Within the boundary layer, we apply (prescribed) large-scale horizontal advective tendencies for temperature (T) and water vapor (Q). The large-scale vertical advection of T and Q is calculated from the (prescribed) large-scale ascent/descent and the vertical gradients of the domain-averaged temperature and moisture profiles [*Grabowski et al.*, 1996]. The horizontal tendencies and the large-scale

ascent/descent are derived from the National Oceanic and Atmospheric Administration Rapid Update Cycle (RUC) data analyses [*Zhang and Lin*, 1997; *Xie et al.*, 2004], and are imposed on the model grid points uniformly in the horizontal domain. Above the boundary layer, a linear combination of the large-scale horizontal advective tendencies and large-scale vertical advection with terms used to nudge the simulation toward the large-scale fields from the variational analysis based on the RUC data (with a relaxation time of 1 hour) is imposed for the T and Q fields. This variational analysis is constrained by the observed surface and top of the atmosphere measurements, and the atmo-
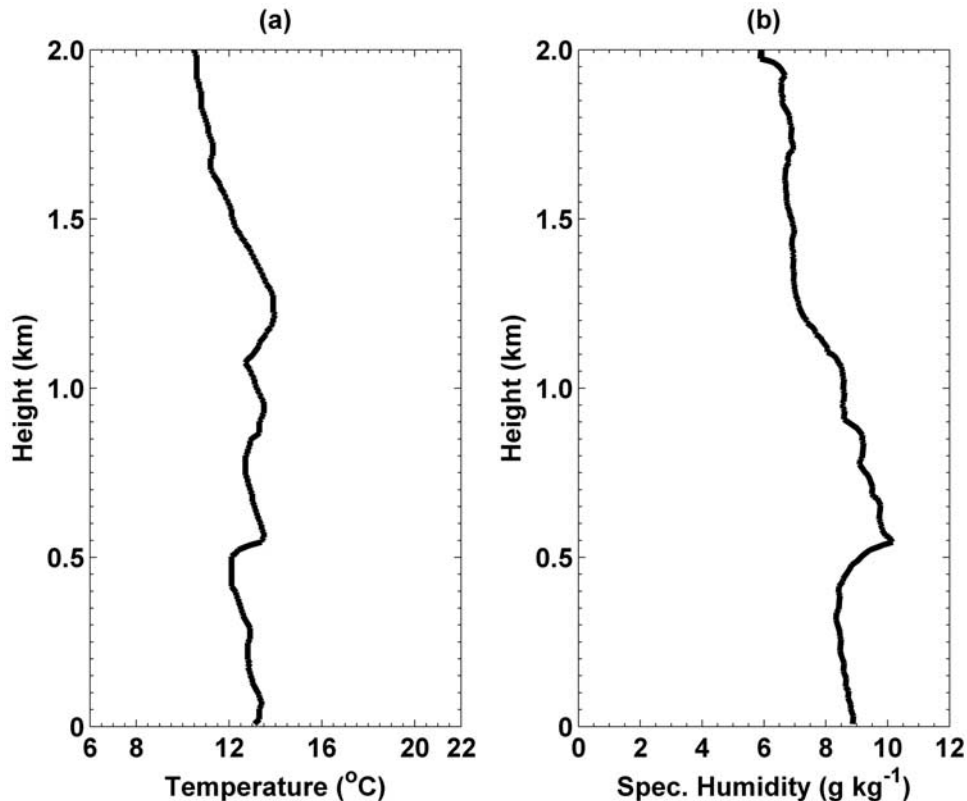

Figure 1. The initial (a) temperature and (b) specific humidity profiles from the radiosonde sounding at 0530 LST on 17 May 2003.
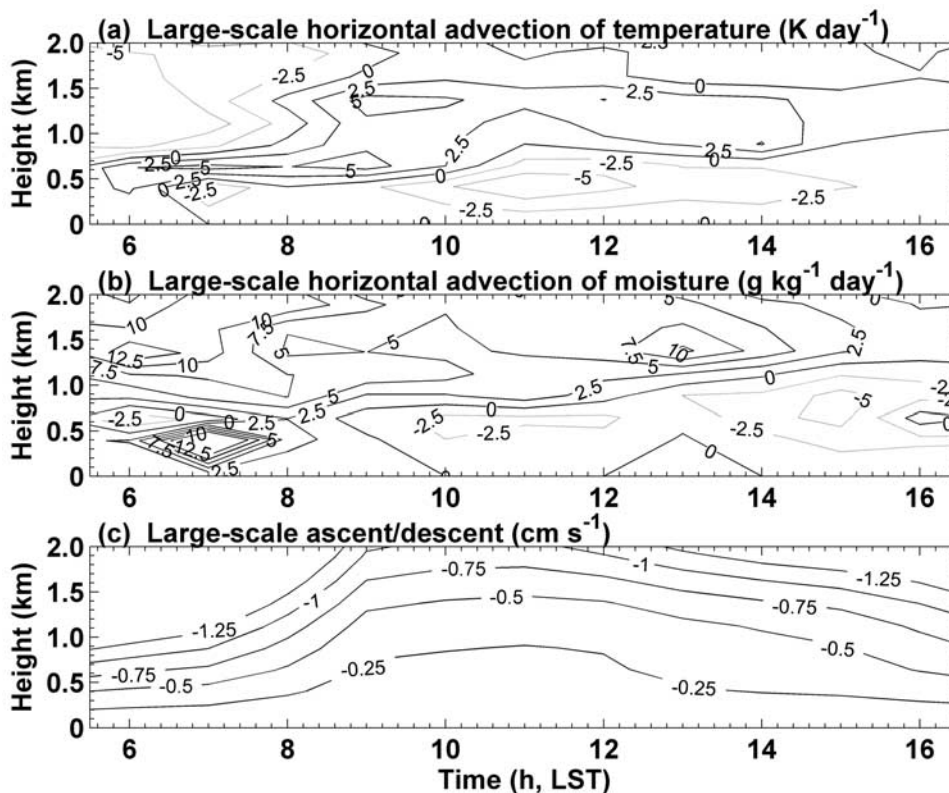
Figure 2. Prescribed temporal evolution of the large-scale horizontal advective tendencies for (a) temperature and (b) moisture, and (c) large-scale ascent/descent derived from the Rapid Update Cycle (RUC) data archive over the Central Facility of the Southern Great Plains (SGP) site on 17 May 2003. Contour intervals are 2.5 K d^{-1} in Figure 2a, 2.5 g kg^{-1} d^{-1} in Figure 2b, and 0.25 cm s^{-1} in Figure 2c.

spheric state variables are adjusted to balance the observed column budgets of mass, heat, moisture, and momentum [*Xie et al.*, 2004]. The horizontally averaged wind component in the east-west direction (U) from ATHAM is also nudged toward the large-scale variational analysis wind field based on the RUC data. The RUC data is available every 1 hour, and is then linearly interpolated to the ATHAM time and height levels.

3. Case Description and Base Case

3.1. Case Description

[21] The case selected for this study is a relatively horizontally homogeneous stratus cloud system observed at the Central Facility (CF) of the SGP site on 17 May 2003 during the AIOP [*Feingold et al.*, 2006]. Light drizzle was observed prior to 1100 local standard time (LST), but some important measurements for our study, for example, the cloud LWP, were only available after 1200 LST. In addition to the routine remote sensing measurements and radiosonde soundings, airborne measurements were also available starting at around 1300 LST. Therefore we compared our simulation results with the available measurements after 1200 LST.

3.2. Base Case

[22] Our model simulations begin at 0530 LST. Initially the boundary layer is relatively stable and capped by a weak inversion layer. Figure 1 shows the initial temperature and

moisture profiles from the radiosonde sounding. Temperature decreases slightly with height from 13.2°C near the surface to 12.2°C at an altitude of 0.5 km. The moisture profile (or specific humidity) exhibits a similar feature. Because of the capping by the inversion layer, moisture is accumulated just below the inversion layer and reaches its maximum near the inversion layer at an altitude of 0.55 km. We assumed that the atmosphere was cloud free at the beginning of our simulations.

[23] Figures 2a and 2b show the large-scale horizontal advective tendencies of temperature and moisture, respectively, based on the RUC data over the Central Facility at the SGP site. At the beginning (from 0530 LST to 0630 LST), there is a weak advection of warm temperatures from the surface up to 0.75 km, and there is advection of colder air above 0.75 km. This advection of warm air is gradually replaced by the advection of cold air near the surface while the advection of cold air aloft is gradually replaced by the advection of warm air. From 0530 LST to 1200 LST, there is a strong advection of moisture into the model domain, especially above 0.75 km, but this is gradually replaced by the advection of drier air. The large-scale subsidence above 1 km is strong in the early morning hours and becomes weaker as daytime progresses (Figure 2c).

[24] The surface sensible and latent heat fluxes are prescribed using the Energy Balance Bowie Ratio (EBBR) station measurements at the CF of the SGP site (Figure 3). Since these measurements are available every half hour,
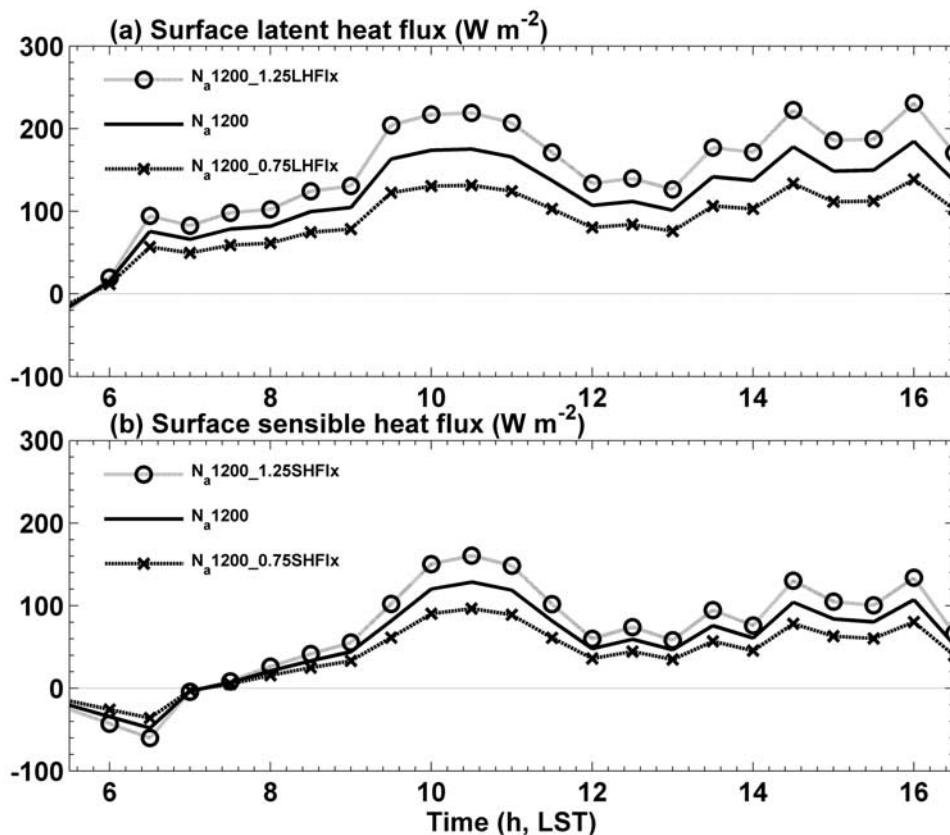
Figure 3. The (a) surface latent and (b) sensible heat fluxes in the base case (N_a1200) from the Energy Balance Bowie Ratio (EBBR) station measurement at the Central Facility (CF) of the SGP site on 17 May 2003; and in the sensitivity tests for an increase (N_a1200_1.25LHFlx) and a decrease (N_a1200_0.75LHFlx) of 25% in the surface latent heat flux; and in the sensitivity tests for an increase (N_a1200_1.25SHFlx) and a decrease (N_a1200_0.75SHFlx) of 25% in the surface sensible heat flux. Line types or markers are indicated in the legend.

they are linearly interpolated to the model time. At 0530 LST, both the surface sensible and latent heat fluxes are negative. As daytime progresses, they become positive and reach a maximum just prior to local noon. These prescribed surface fluxes are imposed in the lowest layer of the model.

[25] The aerosol size distribution was measured by an airborne Passive Cavity Aerosol Spectrometer (PCASP) with a lower particle size cut of 0.1 μm in diameter (Figure 4). Observations of the aerosol chemical composition and loading were also available near ground level. The major chemical component of the aerosols was sulfate. Sulfate was assumed to be internally mixed with other aerosol components, e.g., nitrate, dust, and organic matter. Following *Delene and Deshler* [2001] and *Penner et al.* [2004], we assume that the aerosol mixing ratio is constant with altitude since the water vapor mixing ratio near the cloud base is within 10% of the ground level value as measured by the ARM radiosonde and the airborne measurements (Figures 1 and 5).

3.3. Comparisons With Observations

[26] Model performance was evaluated by comparing the base case model results with observations. Figures 5a and 5b show the vertical profiles of temperature (T) and specific humidity (Q), respectively, from the airborne measurement,
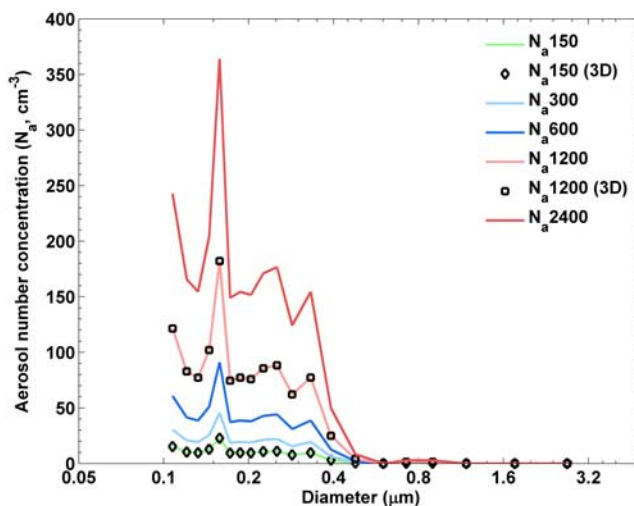

Figure 4. The aerosol particle size distribution from the Passive Cavity Aerosol Spectrometer (PCASP) measurement, which is used in the 2-D and 3-D base case simulations (N_a1200) and N_a1200 (3-D)). Other distributions are used in four 2-D sensitivity tests of N_a150–N_a2400 and in the 3-D sensitivity test N_a150(3-D) (as summarized in Table 1). Line types or markers are indicated in the legend.
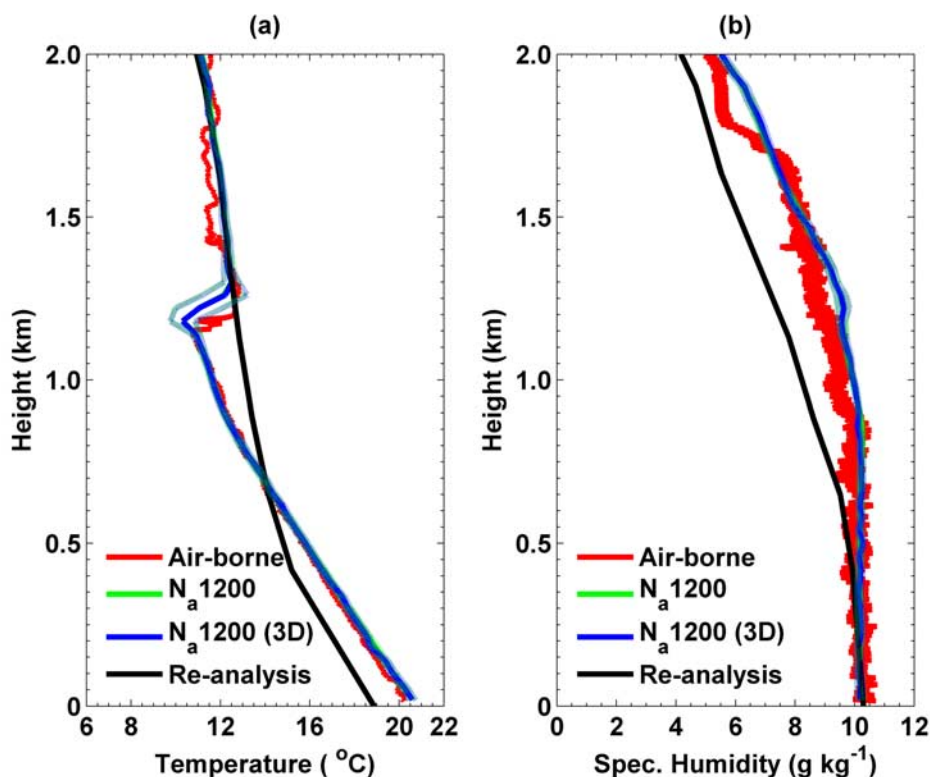
Figure 5. Vertical profiles of the horizontally averaged (a) temperature and (b) specific humidity from the 2-D base case simulation N_a1200 and its standard deviation, from the 3-D base case simulation N_a1200 (3-D) and its standard deviation, from the airborne measurement, and from the large-scale reanalysis based on the RUC data at 1300 LST on 17 May 2003. Line types or markers are indicated in the legend.

from the 2-D simulation, from the 3-D simulation, and from the large-scale reanalysis near 1300 LST. As shown there, 2-D and 3-D results almost overlap with each other, and both simulations are able to capture the inversion layer measured by the airborne measurements reasonably well. Below the inversion layer (at the altitude of 1.2 km above the ground), the predicted temperature profile is almost the same as the observed one. The simulated moisture profile also closely matches the measured profile below the inversion. However, the model fails to capture the sharp decrease in the specific humidity near 1.75 km. One reason for this model behavior is the relatively strong large-scale advection of moisture at this height (Figure 2). The simulated T and Q are much closer to the air borne measurements (which are expected to be more reliable) than to the reanalysis data. The good agreement of the T and Q profiles between the model and observation is critical for the simulation of the cloud morphology and cloud water content (Figure 6).

[27] Figure 6 presents the temporal evolution of cloud water mixing ratio q_c from the 2-D simulation. The q_c increases slightly from 1200 LST to 1300 LST and reaches a maximum of about 0.5 g kg^{-1} near the cloud top. However, this enhancement is dominated by the reduced cloud geometrical thickness (H), so that the LWP decreases monotonically after 1200 LST, as does the COD (Figure 7). The observed COD is retrieved by a nonlinear least squares method using the atmospheric transmittance and the surface
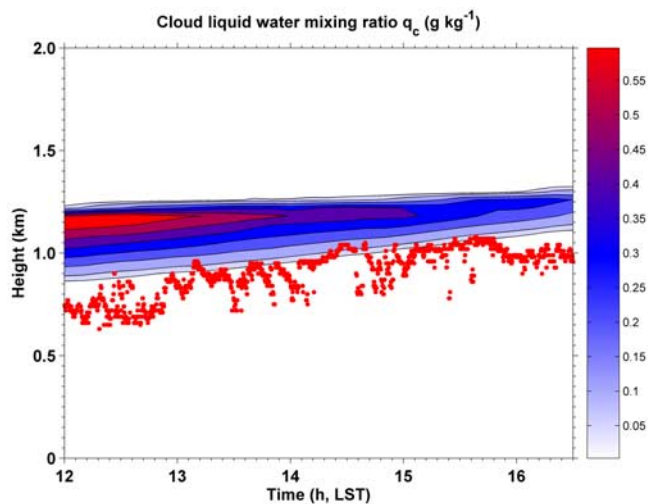

Figure 6. Time-height cross section of the horizontally averaged cloud liquid water mixing ratio (q_c) from the 2-D base case simulation N_a1200. Dots denote the best estimate for the cloud base from the Vaisala Ceilometer (VCEIL) measurement.

albedo obtained from the Multi-Filter Rotating Shadowband Radiometer (MFRSR). The best estimate of the cloud base height from the Vaisala Ceilometer (VCEIL) measurement is also presented. The simulated cloud base and the observed cloud base are in good agreement (Figure 6).

[28] Figure 7 also shows the averaged R_e over cloudy layers from ATHAM, which is calculated from $R_e = \beta \left(\frac{3}{4} \frac{\sum_j \rho q_c}{\sum_j \pi N_d \rho_w} \right)^{\frac{1}{3}}$, where j refers to cloudy cells ($q_c > 0.001$ g kg^{-1} and $N_d > 5$ cm^{-3}). The averaged R_e could also be calculated as the average of the local effective radii over cloudy cells. However, a simulation that evaluated the difference in these two formulations for the base case showed that these two estimates of the averaged R_e are very similar. So we used the former estimate.

[29] Our R_e could be calculated for the same volume as that sampled by the CAPS (Cloud-Aerosol-Precipitation-Spectrometer) instrument, and then it would be appropriate to compare our R_e with the R_e from the CAPS measurement. However, the volume sampled by CAPS is much smaller (7×10^{-6} m^3 [Feingold et al., 2006]) than a single grid of the CRM ($\sim 2 \times 10^6$ m^3), so it is hard to determine which grid of the model to use in the comparison. Moreover, these in situ measurements were limited to the time period of aircraft penetration into cloud layers around 1300 LST, while the MFRSR retrievals provided R_e (under the constraint of the total LWP from Microwave Radiometer (MWR) [Min et al., 1996]) over a much longer time period (1200 LST to 1600 LST). This makes the MFRSR measured R_e more appropriate for validation of the model results. The MFRSR retrieved R_e here is the column average over the observed cloudy domain of a circle with a radius of 1 km within 5 min interval [Min et al., 2001; Feingold et al., 2006]. Min et al. [2003] showed that the MFRSR retrieved R_e for single-layer warm water clouds agrees well with in situ FSSP (Forward Spectra Scattering Probe) measurements to within 5.5%. Feingold et al. [2006] compared the retrieved R_e from five different methods including the MFRSR, in situ CAPS, and the MODIS satellite instrument for the same stratus cloud on 17 May 2003 as in our study, and showed that the retrievals of R_e agreed with one another to within $\sim 20\%$, which is approximately the error estimate for most methods.

[30] As shown in Figure 7, the diurnal variation of COD and R_e are less significant than that of the LWP. The simulated R_e (~ 5.8 μm) is slightly smaller than the retrieved R_e from the MFRSR (~ 6.5 μm). There are no large differences in the temporal evolution of LWP, COD, or R_e between the 2-D and 3-D simulations. This is expected because this stratus cloud is relatively homogeneous and cloud ensemble properties should be similar for 2-D and 3-D simulations [Grabowski et al., 1998; Moeng et al., 2004].

[31] We note here that 2-D simulations will have stronger convection than their 3-D counterparts, because 2-D simulations cascade turbulent energy upscale rather than downscale as in 3-D simulations. As shown by Moeng et al. [1996], the TKE was larger in their 2-D simulations than that in their 3-D simulations (~ 0.7 versus ~ 0.2 m^2 s^{-2} at the middle of planetary boundary layer). However, the vertical velocity variances were similar in the 2-D and 3-D simulations near the cloud base where cloud droplet nucleation occurs; and it is the vertical velocity that matters for the nucleation process. We have verified this in our simulations so are confident that this correspondence explains that the number of activated cloud droplets in our 2-D and 3-D simulations, and other cloud ensemble properties are similar. From their CRM/LES (large eddy simulation) intercomparisons of moist shallow convection, Moeng et al. [1996] pointed out that the cloud structure predicted by the 2-D CRMs was similar to that obtained by the 3-D LES's. Stevens et al. [1998] also pointed out that 2-D models are at least able to qualitatively represent the interaction of the large eddies and microphysical processes in boundary layer flows and can be useful.

[32] The horizontal resolution in our 2-D and 3-D simulations differs (125 m versus 250 m) because of the need to save computer time; but the vertical resolution in both simulations is the same. Obviously the grid-averaged supersaturation depends on the grid size. Changes in resolution could therefore influence the activation of droplets, cloud water content, the onset of precipitation and its amount, and could thereby influence the stability of the subcloud layer and turbulent circulations, which could in turn influence the strength of convection and precipitation itself. As noted by Stevens et al. [1998] when drizzle was active in their simulations, the model results were more sensitive to resolution changes. However, the stratus cloud studied here produced negligible surface precipitation (although there was a small amount of drizzle at cloud base). As a result, turbulent and dynamic feedbacks associated with drizzle are inactive, and thus the simulated cloud characteristics are similar even though the model horizontal resolution varies in our 2-D and 3-D simulations. Stevens et al. [1998] have shown that their domain-averaged LWP changed by <2% after coarsening the resolution (213 g m^{-2} versus 216 g m^{-2} in the control run and the half resolution run, respectively) in their nondrizzling case.

4. Sensitivity Tests
4.1. Sensitivity to Aerosol Number Concentration

[33] One goal of our study was to examine how this cloud responds to changes in the aerosol concentration. Therefore we artificially increased (doubled) and decreased (halved) the aerosol number concentration (N_a) as shown in Table 1 and Figure 4.

4.1.1. First AIE

[34] Figures 8 and 9 show the time series of the spatial averages of N_d, R_e, drizzle rate at cloud base, and LWP in four sensitivity tests and in the base case ("$N_a 1200$"). With increased N_a, the total N_d consistently increases and R_e consistently decreases. Table 1 presents the spatially and temporally averaged N_d ($\overline{N_d}$) and R_e ($\overline{R_e}$) for cloudy cells from 0630 LST to 1630 LST ($\overline{N_d} = \frac{1}{T} \frac{1}{N_{cld}} \int_0^T \sum_j N_d \, dt$ where N_{cld} is the number of cloudy cells; $\overline{R_e} = \beta \left(\frac{3}{4} \frac{\int_0^T \left(\sum_j \rho q_c \right) dt}{\int_0^T \left(\sum_j \pi N_d \rho_w \right) dt} \right)^{\frac{1}{3}}$).

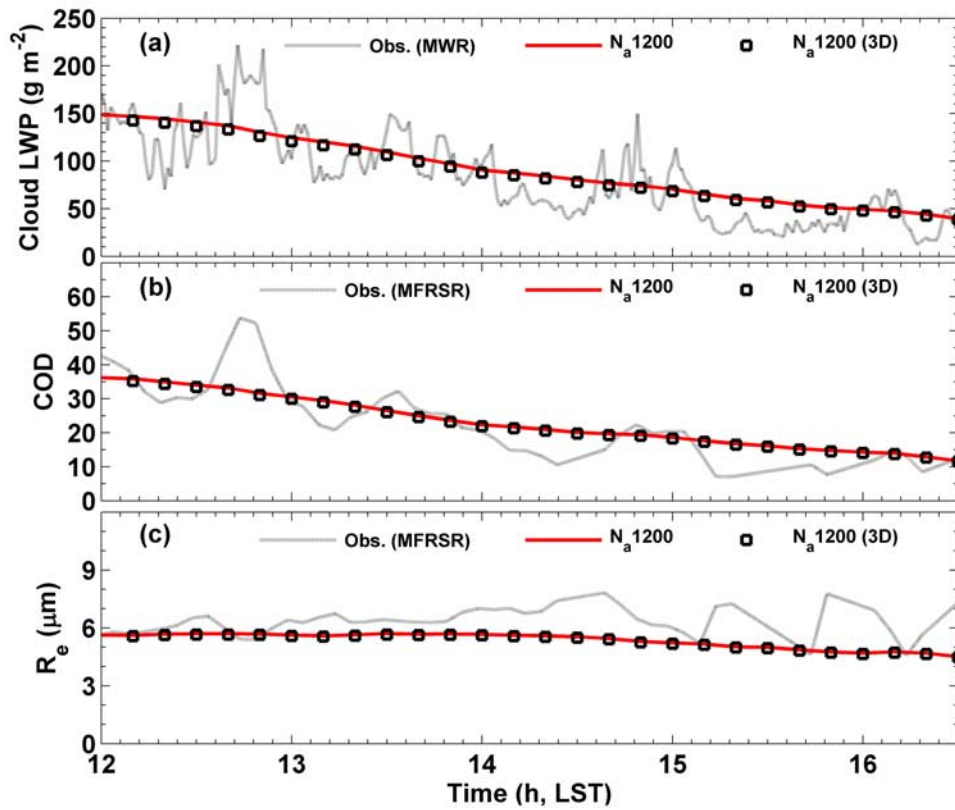Most of the aerosol particles (around 70%) are activated to form cloud drops, especially in the low-N_a cases. This is

Figure 7. Time series of (a) cloud liquid water path (LWP), (b) cloud optical depth (COD), and (c) effective radius (R_e) averaged over cloudy cells from the 2-D base case simulation N_a1200, from the 3-D base case simulation N_a1200 (3-D), and from the measurements. Line types or markers are indicated in the legend.
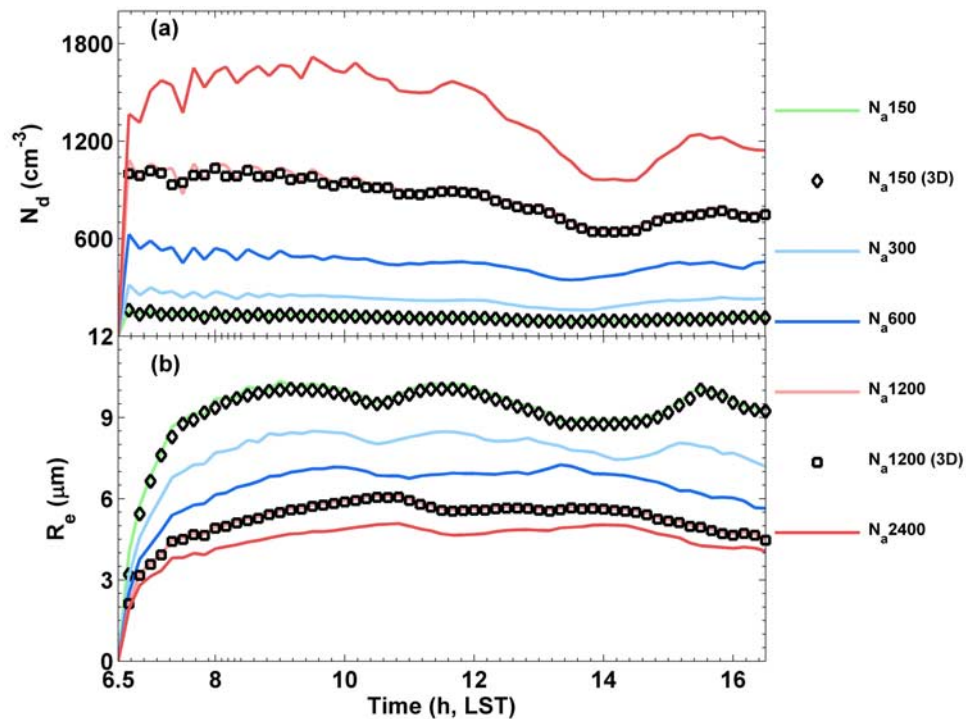

Figure 8. Time series of (a) cloud droplet number concentration (N_d), and (b) effective radius (R_e) averaged over cloudy cells for simulations varying the aerosol number concentration N_a (as summarized in Table 1).
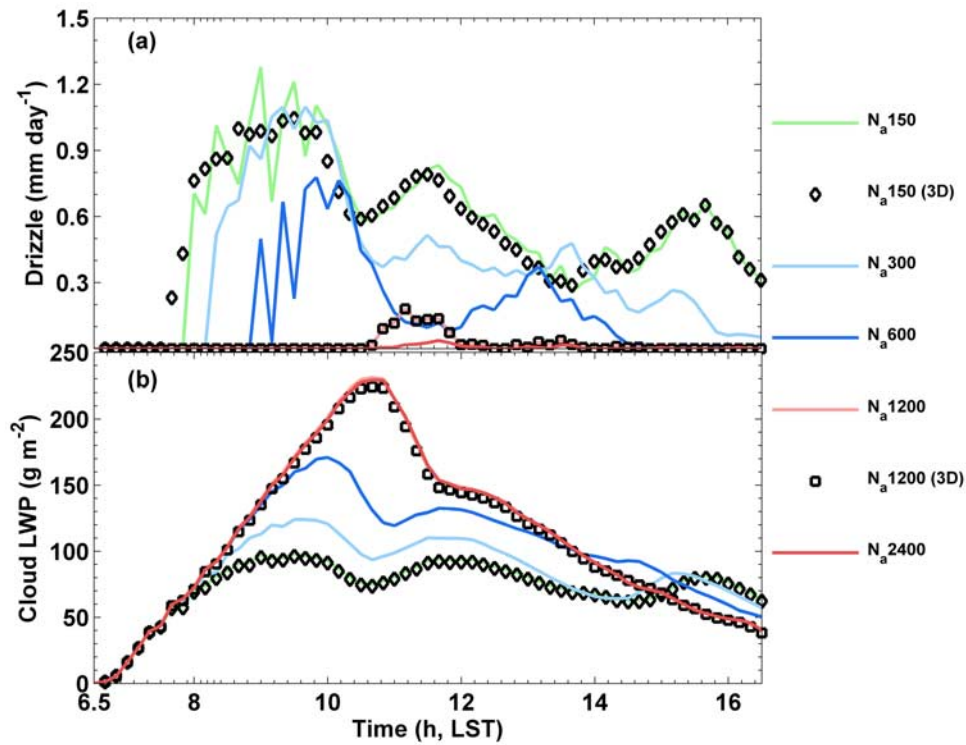
Figure 9. The same as in Figure 8, but for (a) drizzle rate below the cloud base and (b) cloud liquid water path (LWP). (Note: In the 2-D base case simulation N_a1200, the 3-D base case simulation N_a1200 (3-D), and the 2-D sensitivity test N_a2400, the LWPs are almost the same so that three curves overlap.)
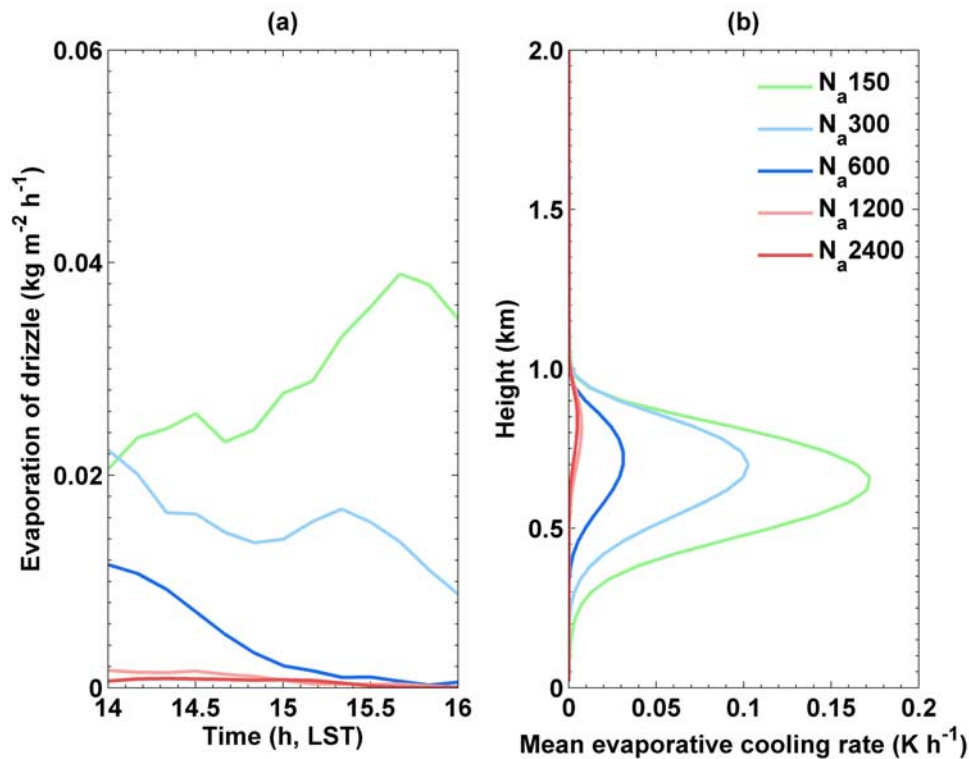

Figure 10. Time series of (a) column-integrated drizzle evaporative rate and (b) profiles of drizzle evaporative cooling rate averaged from 1400 LST to 1600 LST for the 2-D base case simulation N_a1200 and for the four sensitivity tests (N_a150-N_a2400). Line types or markers are indicated in the legend.
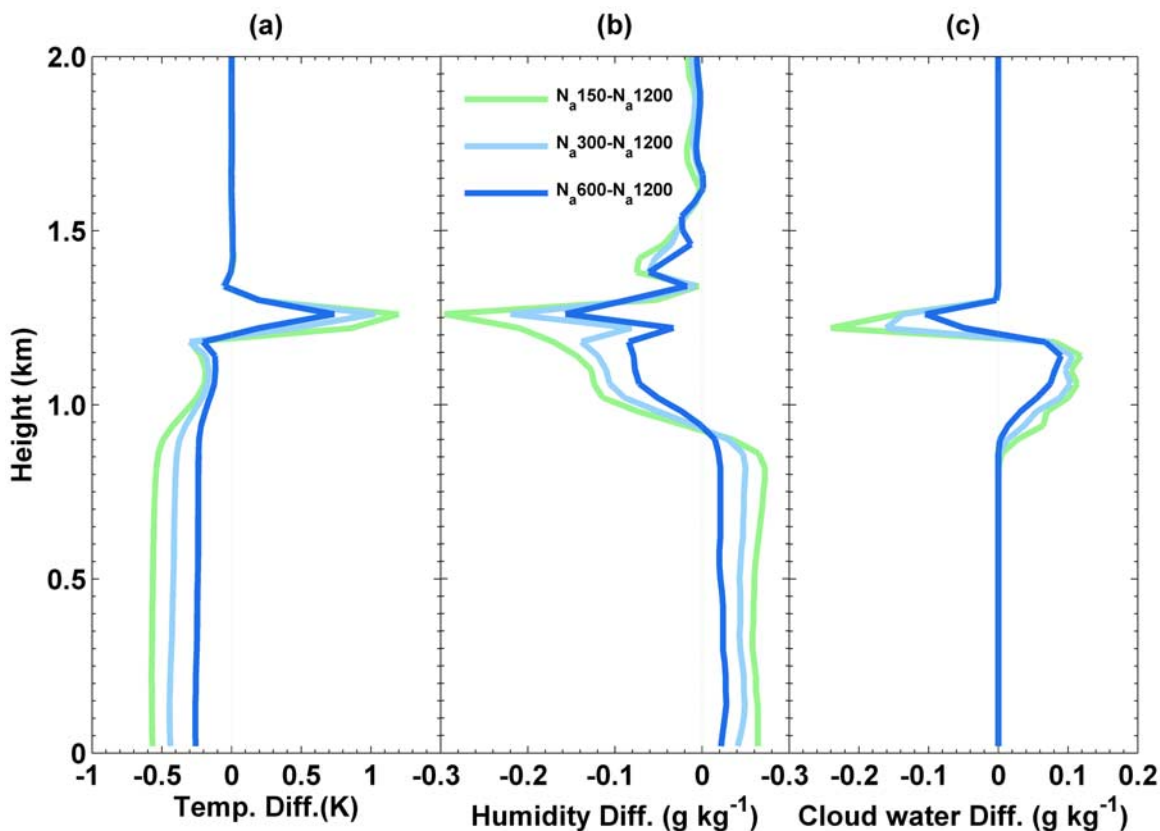
Figure 11. Vertical profiles of the difference in the horizontally averaged (a) temperature, (b) specific humidity, and (c) cloud liquid water mixing ratio (q_c), from 1400 LST to 1600 LST, between the sensitivity test N_a600 and the base case N_a1200, between the sensitivity test N_a300 and the base case N_a1200, and between the sensitivity test N_a150 and the base case N_a1200. Line types or markers are indicated in the legend.

because most of the measured aerosol particles are in the accumulation mode and can readily nucleate (the lower size limit of the PCASP measurement is 0.1 μm in diameter). $\overline{R_e}$ is reduced by 17% when N_a is doubled. The first AIE is evident and generally robust throughout the simulation period (Figure 8 and Table 1).

[35] We note that the total N_d in the base case ("N_a1200") is ∼800 cm^{-3}, while the airborne FSSP measurement showed N_d of 400–500 cm^{-3} (see Appendix A). This discrepancy might be due to the particle size range in the FSSP which does not measure droplets with diameter (D_P) less than 2.4 μm (details of the measured concentrations from the FSSP and CAPS instruments appear in Appendix A).

4.1.2. Second AIE

[36] The second indirect effect involves the response of the cloud macrophysical properties to changes in aerosols. Here, we examine changes in LWP for the time period prior to 1400 LST and after this time.

4.1.2.1. LWP Prior to 1400 LST

[37] Prior to 1400 LST, the LWP generally increases with increases in aerosol concentration (Figure 9 and Table 1). However, because the base case ("N_a1200") is already heavily polluted with little drizzle formation, the spatially and temporally averaged LWP ($\overline{LWP}$) is almost unchanged with a further increase of N_a (compare "N_a1200" with

130.18 g m^{-2} and "N_a2400" with 130.46 g m^{-2}). There is about a 20% decrease of $\overline{LWP}$ when N_a is reduced by half ("N_a600") and this decrease continues when N_a is reduced further ("N_a300" and "N_a150"). The drizzle rate below the cloud base generally decreases as N_a increases. For this case and during this period of time, we find that precipitation below cloud base needs to be higher than about 0.2 mm d^{-1} in order to increase the cloud LWP with increases in N_a. This is similar to the findings reported by *Ackerman et al.* [2004].

4.1.2.2. LWP After 1400 LST

[38] As noted in section 1, satellite observations suggest that the change in LWP with changes in N_a is either neutral or slightly negative for continental clouds when the satellite overpass time is between 1400 LST to 1600 LST [*Han et al.*, 1994, 2002]. This negative/neutral response of the LWP to aerosols is also reproduced in the cloud studied here (Table 1 and Figure 9). The LWP tends to decrease with increases in N_a after 1400 LST. The LWP in the cleanest case ("N_a150") becomes highest after 1500 LST (positive second AIE).

[39] This positive second AIE is associated with drizzle evaporative cooling. Figure 10a shows the time series of the column-integrated evaporation rate by the falling drizzle. Obviously, "N_a150" has the strongest drizzle evaporation rate because it has the highest drizzle production. The
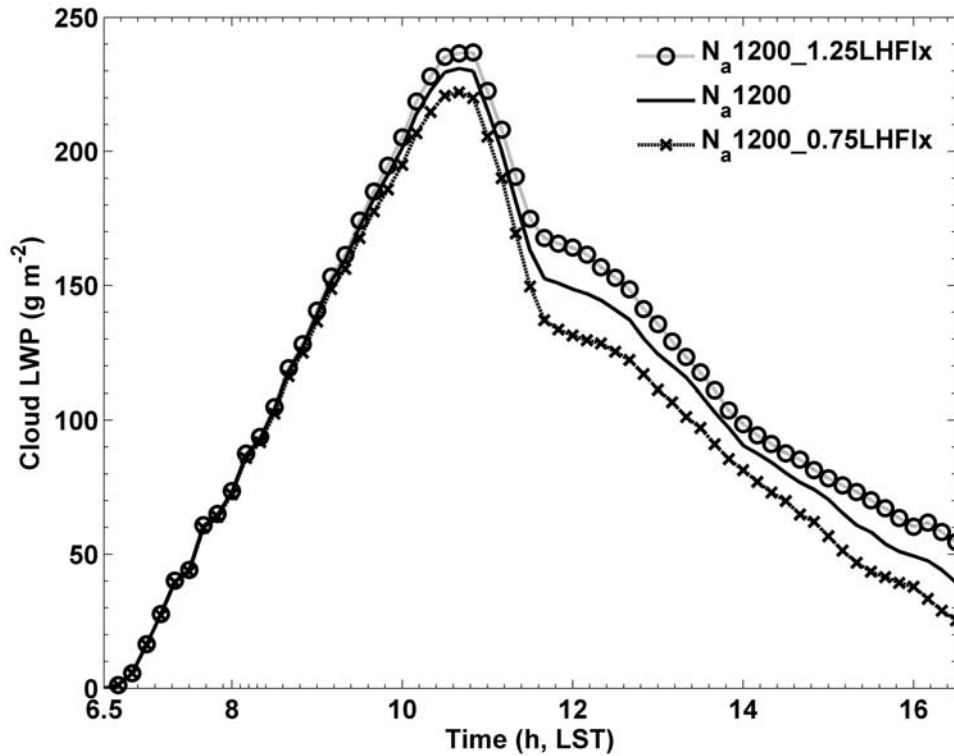
Figure 12. Time series of the cloud liquid water path (LWP) in the 2-D base case simulation (N_a1200), and in the 2-D sensitivity tests for increasing ($N_a1200\_1.25LHFlx$) and decreasing ($N_a1200\_0.75LHFlx$) the surface latent heat flux by 25%. Line types or markers are indicated in the legend.

vertical profiles of the evaporative cooling rate averaged from 1400 LST to 1600 LST are presented in Figure 10b. Within the subcloud layer (from ∼300 m to ∼1000 m), there is a significant evaporative cooling rate of up to 0.17 K h^{-1} for "N_a150". Therefore the subcloud layer in "N_a150" is expected to be the coldest.

[40] Figure 11a shows the difference in the horizontally and temporally averaged temperature profiles from 1400 to 1600 LST between the sensitivity tests for "N_a150", "N_a300", and "N_a600" with "N_a1200". (Note: The temperature and moisture profiles for "N_a2400" are almost identical to those for "N_a1200" and are therefore omitted for clarity.) The temperatures at cloud base for "N_a150", "N_a300", and "N_a600" are lower than that for "N_a1200" by 0.24 K, 0.21 K, and 0.10 K, respectively. Therefore more water vapor condenses to form cloud water and water vapor content decreases. The horizontally and temporally averaged specific humidity just above cloud base for "N_a150", "N_a300" and "N_a600" is smaller than that for "N_a1200"

by 0.15 g kg^{-1}, 0.13 g kg^{-1}, and 0.07 g kg^{-1}, respectively (Figure 11b), and the horizontally and temporally averaged q_c is larger by 0.10 g kg^{-1}, 0.09 g kg^{-1}, and 0.07 g kg^{-1}, respectively. Near cloud top, however, q_c is smaller than that for "N_a1200".

[41] During the afternoon, the cloud top longwave radiative cooling is largely offset by solar heating, which decreases convective mixing [Ackerman et al., 2004] and reduces the cloud water content near cloud top (Figure 6). This reduced cloud water content, in turn, mitigates the cloud top longwave radiative cooling further. This positive feedback involving cloud water and radiative cooling [Stevens et al., 2001] during the afternoon decreases the difference in q_c near the cloud top (∼1.25 km) between the "N_a1200", "N_a600", "N_a300" and "N_a150" cases (Figure 11). Drizzle evaporative cooling in cases with smaller N_d leads to an increase in the cloud water content in the lower cloudy layers that dominates the decrease of the cloud water

Table 2. Spatial and Temporal Averages From 0630 LST to 1630 LST Over Cloudy Cells for Increasing and Decreasing Surface Fluxes From 2-D Simulations

| Case | Surface Flux | | In-Cloud $\overline{LWP}$, g m^{-2} | $\overline{R_e}$, μm | $\overline{H}$, km | $\overline{CLWC}$, g m^{-3} |
	Latent	Sensible				
$N_a1200\_1.25LHFlx$	×1. 25	×1.	120.25	5.38	0.30	0.36
$N_a1200\_0.75LHFlx$	×0.75	×1.	104.46	5.16	0.28	0.33
$N_a1200\_1.25SHFlx$	×1.	×1.25	89.00	4.93	0.27	0.29
$N_a1200\_0.75SHFlx$	×1.	×0.75	119.61	5.57	0.35	0.33
N_a1200	×1.	×1.	113.16	5.29	0.29	0.34

content in the upper cloud layers. Hence the LWP tends to increase as the N_a decreases.

[42] As shown in Figures 8 and 9, the response of the 3-D model closely matches that of the 2-D model, but the 3-D results tend to be somewhat smoother as seen especially in the drizzle results (Figure 9a).

[43] We also explored two other sensitivity tests in which drizzle evaporation was inactivated ("N$_a$1200_no_evap" and "N$_a$150_no_evap" in Table 1). From 1400 LST to 1600 LST, as well as during the earlier simulation period (from 0630 LST to 1400 LST), LWP is consistently larger in "N$_a$150_no_evap" (Table 1).

4.2. Sensitivity Tests for Surface Fluxes

[44] We applied the measured surface latent and sensible fluxes in the base case (section 3) and in the sensitivity tests for changes in N_a (section 4.1). In this section, we artificially increased/decreased these fluxes by 25% in order to examine the effect of the surface forcing. In a fully coupled atmosphere-surface system, the surface fluxes would adjust themselves according to the evolution of the temperature and moisture vertical profiles [*Feingold et al.*, 2005], but this might mask the impact of changes in droplet concentrations on the continental boundary layer and on the clouds of interest here.

4.2.1. Surface Latent Heat Flux

[45] The sensitivity tests for increasing and decreasing the surface latent heat flux are referred as "N$_a$1200_1.25LHFlx" and "N$_a$1200_0.75LHFlx". As expected, a larger surface latent heat flux leads to a higher cloud LWP, and vice versa (Figure 12). The spatial and temporal average of LWP increases (decreases) by 7% in "N$_a$1200_1.25LHFlx" ("N$_a$1200_0.75LHFlx") w.r.t. "N$_a$1200" (Table 2). In both "N$_a$1200_1.25LHFlx" and "N$_a$1200_0.75LHFlx", there is little drizzle production; and therefore any feedback from drizzle evaporative cooling is absent. Since the subcloud layer is well mixed (Figure 5), the surface moisture flux is effectively transported upward. As a result, the LWP responds almost linearly to the increased (decreased) surface latent heat flux.

[46] Table 2 presents the spatial and temporal averages (from 0630 LST to 1630 LST) of the cloud geometrical thickness ($\bar{H}$) and cloud liquid water content ($\overline{CLWC}$). Both $\bar{H}$ and $\overline{CLWC}$ increase/decrease almost linearly (by 3–4%) in "N$_a$1200_1.25LHFlx"/"N$_a$1200_0.75LHFlx"). A higher-surface latent heat flux not only increases the cloud moisture, but also slightly deepens the cloud layer proportionally.

4.2.2. Surface Sensible Heat Flux

[47] Over land, both surface sensible and latent heat fluxes undergo a significant diurnal variation because land surfaces respond quickly to the solar heating. Two sensitivity tests for increasing and decreasing the surface sensible heat flux by 25% were also carried out ("N$_a$1200_1.25SHFlx" and "N$_a$1200_0.75SHFlx" in Table 2). Figure 13 shows the time series of the horizontally averaged in-cloud LWP and cloud fraction. An enhanced surface sensible heat flux helps "evaporate" clouds and leads to a reduction of both the in-cloud LWP and cloud fraction. Figure 14 presents the temporal evolution of the cloud liquid water mixing ratio q_c. Between 0630 LST and 1400 LST, the magnitude of q_c and its spatial pattern are similar, but the cloud tends to be

shallower in "N$_a$1200_1.25SHFlx". Both the cloud top and cloud base rise faster in "N$_a$1200_1.25SHFlx" (Figure 15). From 0700 LST to 1400 LST the cloud base rises from 0.5 km to 1.0 km and cloud top rises from 0.5 km to 1.3 km. (Note: The cloud base and top in ATHAM are defined as the lowest and highest model levels with the cloud water mixing ratio (q_c) > 0.001 g kg^{-1} and N_d > 5 cm^{-3}). However, over the same period in "N$_a$1200_0.75SHFlx", the cloud base rises from 0.5 km to 0.8 km and cloud top rises from 0.5 km to 1.3 km. The difference between the cloud tops is less pronounced than the difference between the cloud bases in the two cases, and hence the cloud is much shallower in "N$_a$1200_1.25SHFlx". A higher-surface sensible flux gives rise to a deeper subcloud layer (i.e., an increased cloud base), and leads to a lower LWP [*Golaz et al.*, 2001]. As shown in Table 2, $\overline{CLWC}$ is reduced by only 10% from "N$_a$1200_0.75SHFlx" to "N$_a$1200_1.25SHFlx". However, $\bar{H}$ is reduced by 23%, and the in-cloud LWP is reduced by 26%. The change in the LWP is mainly attributed to the change in H.

[48] As daytime progresses, the relative humidity (RH) below and above cloud becomes lower in "N$_a$1200_1.25SHFlx" than in "N$_a$1200_0.75SHFlx" (Figure 16). Stronger surface sensible heat supply in "N$_a$1200_1.25SHFlx" leads to a warmer and drier subcloud layer (lower ambient RH). Moreover, drier air is entrained from above into cloud layer and depletes cloud water [*Ackerman et al.*, 2004]. As a result, the uniform cloud deck is broken up near the end of the simulation (Figure 14), and the cloud fraction is reduced sharply from 100% to 60% from 1400 LST to 1630 LST.

[49] On the average, the in-cloud LWP decreases from 113.36 g m^{-2} to 89 g m^{-2} (by 21%) after increasing the surface sensible heat flux by 25%. This decrease is similar to that caused by quadrupling N_a (Tables 1 and 2), and is mainly due to the change of cloud morphology (especially cloud base) and the drier subcloud layer (Figures 15 and 16). Therefore the response of LWP to surface sensible heat flux is even more striking than its response to aerosols.

5. Conclusions and Discussion

[50] In this continental stratus cloud case, 2-D and 3-D ATHAM results compare well with observations, e.g., the cloud temporal evolution. The good agreement between the predicted and observed cloud morphology mainly results from the good agreement between the predicted and observed temperature and moisture profiles.

[51] In this study, an increase in aerosol number concentration (N_a) generally resulted in an increase in droplet number concentration (N_d) and a decrease in droplet size. If N_a is high, as in the polluted base case, the precipitation is already very low (or negligible), and an increase in N_a does not change cloud water content or cloud geometrical thickness. During the early part of the day (before 1400 LST), the cloud LWP increases with N_a when there is a significant amount of precipitation (>0.2 mm d^{-1}). This is because the precipitation is an important sink of cloud water for precipitating clouds and its decrease with an increase in N_a allows the LWP to increase.

[52] After 1400 LST, the LWP generally decreases with increases in N_a (positive second indirect effect). The re-
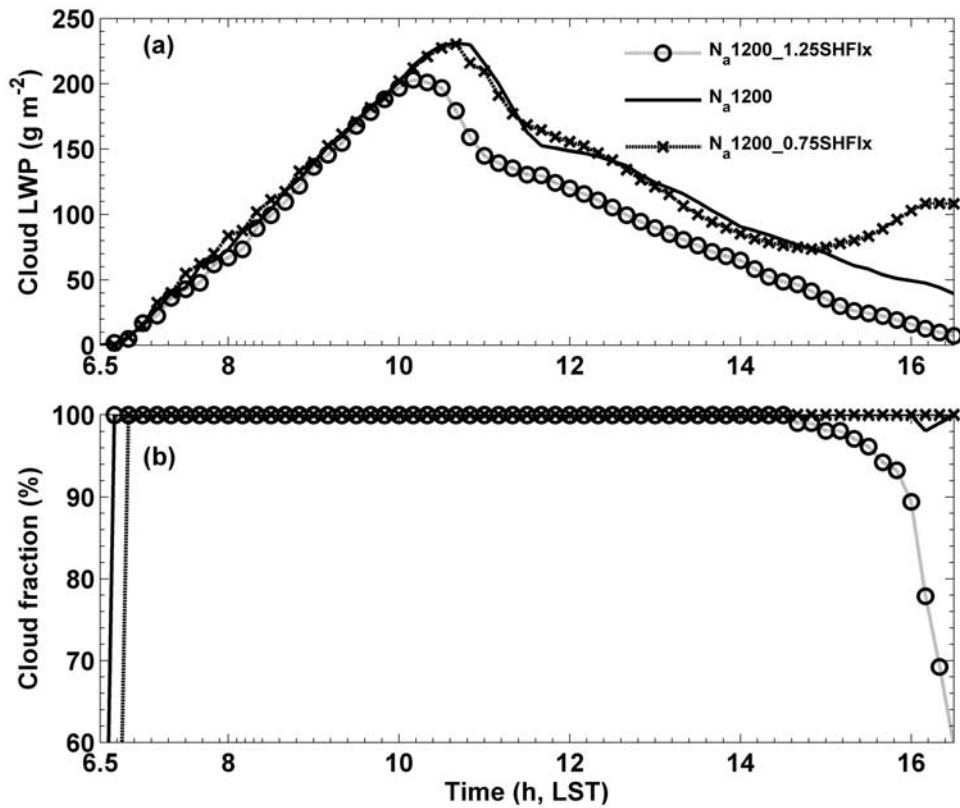
Figure 13. Time series of the in-cloud liquid water path (LWP) and cloud fraction in the 2-D base case simulation (N_a1200), and in the 2-D sensitivity tests for increasing (N_a1200_1.25SHFlx) and decreasing (N_a1200_0.75SHFlx) the surface sensible heat flux by 25%. Line types or markers are indicated in the legend.
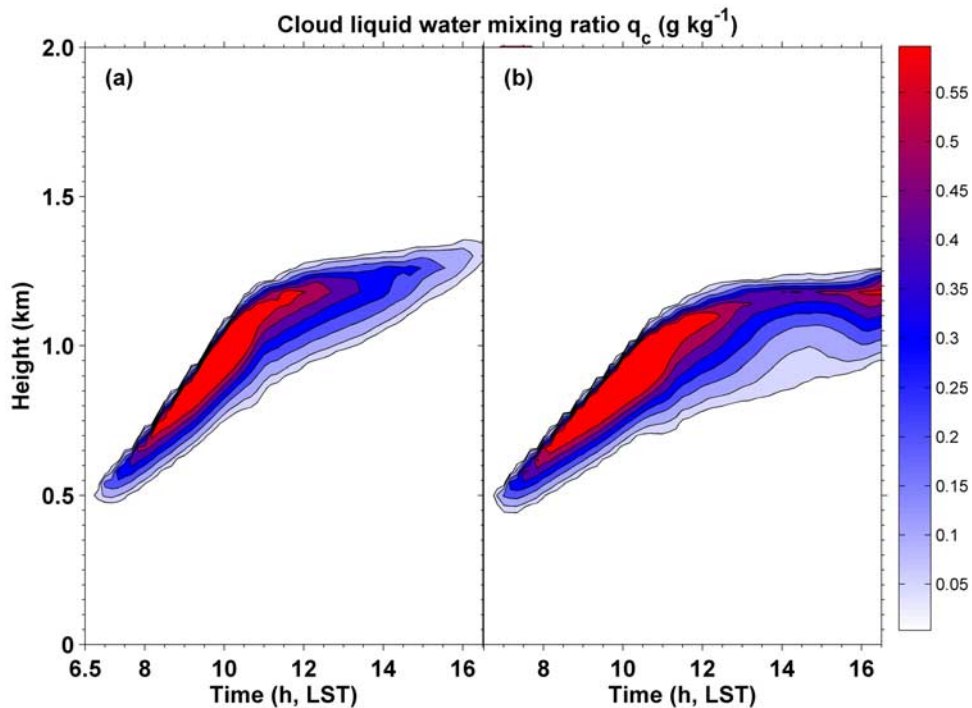

Figure 14. Time-height cross section of the cloud liquid water mixing ratio (q_c) in the 2-D sensitivity tests with (a) increasing (N_a1200_1.25SHFlx) and (b) decreasing (N_a1200_0.75SHFlx) the surface sensible heat flux by 25%.
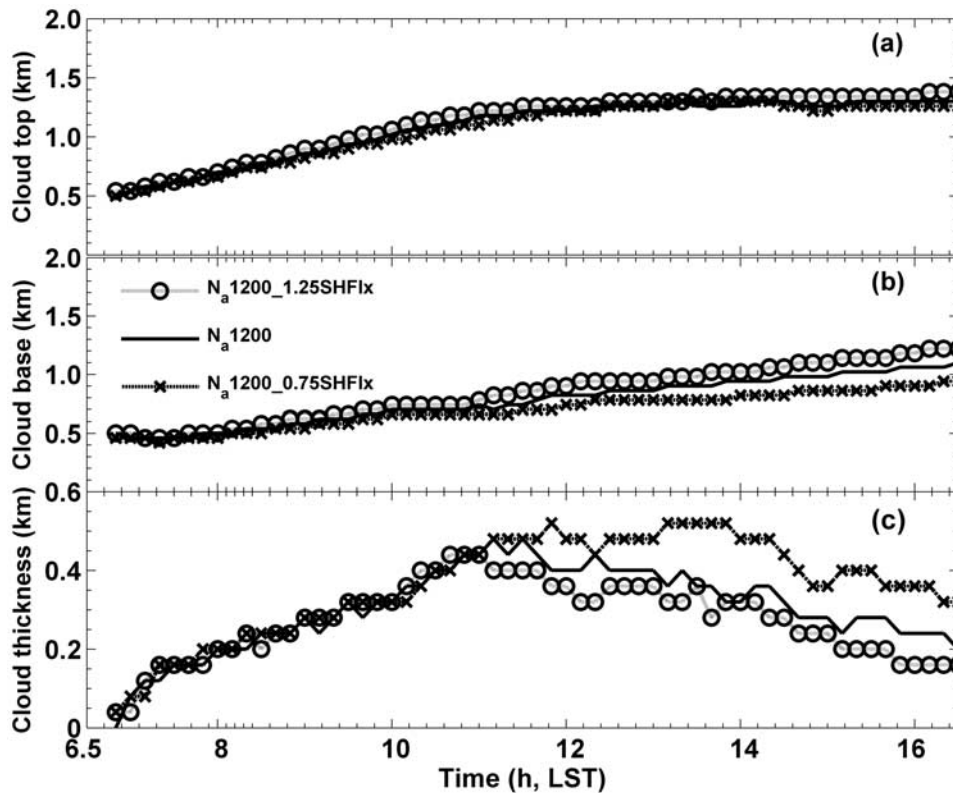
Figure 15. Time series of (a) cloud top, (b) cloud base, and (c) cloud (geometrical) thickness in the 2-D base case simulation (N_a1200), and in the 2-D sensitivity tests with increasing ($N_a1200\_1.25SHFlx$) and decreasing ($N_a1200\_0.75SHFlx$) the surface sensible heat flux by 25%. Line types or markers are indicated in the legend.

sponse of the cloud to changes in aerosol concentration after 1400 LST agrees with satellite observations for continental clouds that show a neutral or slightly negative liquid water sensitivity to cloud drop number concentration [*Han et al.*, 2002]. We explained this by the offset of the longwave radiative cooling near cloud top by solar heating (as daytime progresses) leading to a reduction of cloud water near cloud top. The positive feedback involving radiative cooling and cloud water mitigates the cloud water difference near cloud top caused by different aerosol concentrations. Consequently, drizzle evaporative cooling in the lower part of the cloud leads to more vapor condensation and thereby increases the total LWP when droplet number decreases. Therefore the (second) indirect effect might be smaller than previously thought if this offset occurs frequently in boundary layer clouds. However, this result might be case-dependent and needs to be further explored and examined.

[53] In this case study, the subcloud layer is well mixed and the surface moisture supply is effectively transported upward. As a result, the LWP responds almost linearly to a change of the surface latent heat flux. Both the cloud geometrical thickness and cloud water content increases nearly linearly given a stronger surface latent heat flux.

[54] Surface sensible heat flux plays an important role in the PBL, and influences the growth of cloud base. Sensitivity tests show that the cloud base rises faster than the cloud top with a higher sensible heat flux; and therefore the cloud tends to be shallower (and drier). The impact of

the surface sensible heat flux on the cloud morphology is more pronounced than its impact on the cloud water content. The decrease in the LWP that accompanied an increase in the sensible heat flux by 25% is comparable to the change after quadrupling N_a. The increase in the surface sensible heat flux also leads to a decrease in the cloud fraction toward the end of the day. The uniform cloud deck is broken up as a result of the lower ambient relative humidity.

[55] In this study, we have not coupled the response of surface fluxes to changes in aerosols and clouds, but instead have prescribed surface fluxes on the basis of observations. However, this is not expected to change our results qualitatively. The temperature and specific humidity within the subcloud layer only change by about 0.2 K and 0.02 g kg^{-1} (Figure 11) after doubling aerosol concentrations, respectively. This would not introduce significant changes in surface fluxes and lead to qualitatively different conclusions.

[56] The response of the LWP to aerosols is complicated by thermodynamical feedbacks (e.g., cloud top entrainment, drizzle evaporative cooling and moistening, and surface fluxes), and can sometimes be controlled by them. Moreover, the surface latent and sensible fluxes play an important role in determining the LWP. Anthropogenic emissions of aerosols and their precursors could attenuate the incoming solar radiation and result in a reduction of solar heating at the surface ("solar dimming"). Such a reduction may result in a smaller surface energy and moisture flux transported
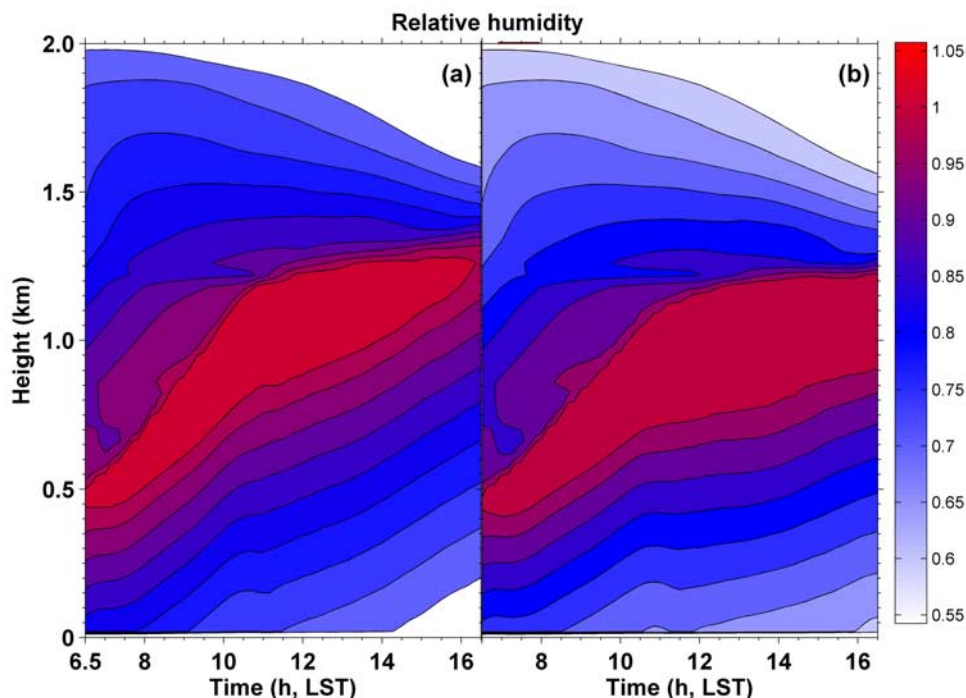
Figure 16. Time-height cross section of the horizontally averaged relative humidity in the 2-D sensitivity tests with (a) increasing (N$_a$1200_1.25SHFlx) and (b) decreasing (N$_a$1200_0.75SHFlx) the surface sensible heat flux by 25%.

upward to the lower atmosphere. These two factors have two competing impacts on the LWP and therefore can either amplify or diminish the total aerosol indirect effect. A decrease in the latent heat flux could lead to a shallower and drier cloud (smaller LWP). A decrease in the sensible heat fluxes could result in a deeper cloud (larger LWP). Since surface latent and sensible flux often covary with each other, and correlate with the underlying surface temperature and soil moisture, a fully coupled atmospheric and the land surface model is needed to investigate further the net effect of aerosols on clouds and the energy budget. Nevertheless, increasing or decreasing surface fluxes as in this study is a useful first step to explore the effect of surface forcing on cloud evolution.

[57] The numerical domain (20 km) in our simulations is much deeper than employed by many models that are used to study boundary layer clouds and aerosol effects. A model top of about 2 km would be desirable, but with the current numerical scheme, a lid of 2 km leads to instabilities that cannot be avoided without introducing damping that corrupts the solution. Thus although the current model configuration gives us results that we trust, future work needs to improve the model numerical schemes in order to achieve both accuracy and efficiency.

Appendix A

[58] Both the CAPS (Cloud Aerosol Precipitation Spectrometer) and the FSSP (Forward Scattering Spectrometer Probe) provide in situ measurements of particle size distribution. CAPS measures particles from 0.6 to 100 μm in diameter and the FSSP measures particles from 2.4 to 51 μm in diameter. Figure A1 shows the particle number concen-

tration from the CAPS and the FSSP measurements around 1300 LST or 1900 UTC. As shown there, the droplet number concentration (N_d) reaches $\sim$1200 cm^{-3} around 1305:24 LST near the cloud base from the CAPS measurement if we regard particles with diameter (D$_P$) from 1.5 μm to 54 μm as cloud droplets; but N_d is only $\sim$500 cm^{-3} from the FSSP measurement at the same time. This disagrees with the presentation of N_d by *Feingold et al.* [2006, Figure 3a]:
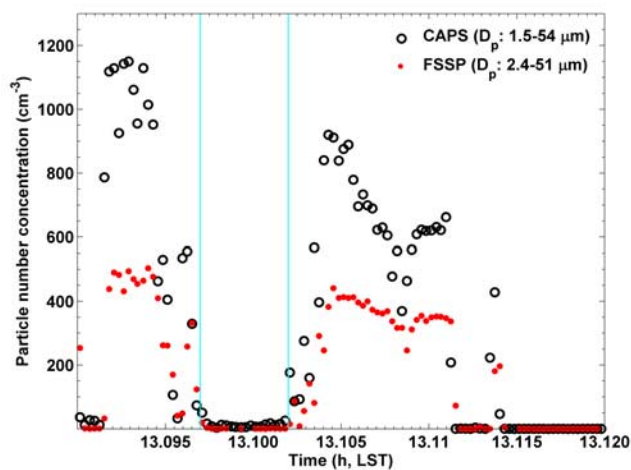

Figure A1. In situ measurements of particle number concentration from the Cloud Aerosol Precipitation Spectrometer (CAPS) and the Forward Scattering Spectrometer Probe (FSSP) measurements around 1300 LST (or 1900 UTC).

Their Figure 3a is similar to our Figure A1 from the FSSP measurement. The difference in droplet number concentration from the two measurements is partly associated with the FSSP detection threshold (2.4 μm in diameter), which is particularly a problem in polluted clouds [*Brenguier et al.*, 2003].

[59] From 1305:49 LST to 1306:11 LST, N_d is close to 0 cm^{-3} from both the CAPS and the FSSP measurements. We suspect that during this period the aircraft traversed into a clear region (personal communication with Haflidi Jonsson, 2007).

[60] The average N_d from in situ measurements is $\sim$700–800 cm^{-3} around 1300 LST if the smaller droplets from the CAPS measurement are included, which is comparable to our model results ($N_d \sim 800$ cm^{-3}).

References

Abdul-Razzak, H., and S. Ghan (2002), A parameterization of aerosol activation: 3. Sectional representation, *J. Geophys. Res.*, *107*(D3), 4026, doi:10.1029/2001JD000483.

Ackerman, A. S., O. B. Toon, D. E. Stevens, and J. A. Coakley Jr. (2003), Enhancement of cloud cover and suppression of nocturnal drizzle in stratocumulus polluted by haze, *Geophys. Res. Lett.*, *30*(7), 1381, doi:10.1029/2002GL016634.

Ackerman, A. S., M. P. Kirkpatrick, D. E. Stevens, and O. B. Toon (2004), The impact of humidity above stratiform clouds on indirect aerosol climate forcing, *Nature*, *432*, 1014–1017.

Albrecht, B. A. (1989), Aerosols, cloud microphysics, and fractional cloudiness, *Science*, *243*, 1227–1230.

Beheng, K. (1994), A parameterization of warm cloud microphysical conversion processes, *Atmos. Res.*, *33*, 207–233.

Brenguier, J.-L., H. Pawlowska, L. Schuller, R. Preusker, J. Fischer, and Y. Fouquar (2000), Radiative properties of boundary layer clouds droplet effective radius versus number concentration, *J. Atmos. Sci.*, *57*, 803–821.

Brenguier, J.-L., H. Pawlowska, and L. Schuller (2003), Cloud microphysical and radiative properties for parameterization and satellite monitoring of the indirect effect of aerosol on climate, *J. Geophys. Res.*, *108*(D15), 8632, doi:10.1029/2002JD002682.

Chou, M., M. Suarez, X. Liang, and M.-H. Yan (2001), A thermal infrared radiation parameterization for atmospheric studies, *NASA Tech. Rep. on Global Modeling and Data Assimilation, NASA/TM-2001-104606, 19,* 68 pp.

Delene, D. J., and T. Deshler (2001), Vertical profiles of cloud condensation nuclei above Wyoming, *J. Geophys. Res.*, *106*, 12,579–12,588.

Feingold, G., H. Jiang, and J. Y. Harrington (2005), On smoke suppression of clouds in Amazonia, *Geophys. Res. Lett.*, *32*, L02804, doi:10.1029/2004GL021369.

Feingold, G., R. Furrer, P. Pilewskie, L. A. Remer, Q. Min, and H. Jonsson (2006), Aerosol indirect effect studies at Southern Great Plains during the May 2003 Intensive Operations Period, *J. Geophys. Res.*, *111*, D05S14, doi:10.1029/2004JD005648.

Ferrare, R., G. Feingold, S. Ghan, J. Ogren, B. Schmid, S. E. Schwartz, and P. Sheridan (2006), Preface to special section: Atmospheric Radiation Measurement Program May 2003 Intensive Operations Period examining aerosol properties and radiative influences, *J. Geophys. Res.*, *111*, D05S01, doi:10.1029/2005JD006908.

Garstang, M., and D. R. Fitzjarrald (1999), *Observations of Surface to Atmosphere Interactions in the Tropics*, Oxford Univ. Press, New York.

Golaz, J.-C., H. Jiang, and W. R. Cotton (2001), A large-eddy simulation of cumulus clouds over land and sensitivity to soil moisture, *Atmos. Res.*, *59-60*, 373–392.

Grabowski, W. W. (2006), Indirect impact of atmospheric aerosols in idealized simulations of convective-radiative quasi-equilibrium, *J. Clim.*, *19*, 4664–4682.

Grabowski, W. W., X. Wu, and M. W. Moncrieff (1996), Cloud resolving modeling of tropical systems during Phase III of GATE. part I: Two-dimensional experiments, *J. Atmos. Sci.*, *53*, 3684–3709.

Grabowski, W. W., X. Wu, M. W. Moncrieff, and W. D. Hall (1998), Cloud resolving modeling of tropical systems during Phase III of GATE. part II: Effects of resolution and the third spatial dimension, *J. Atmos. Sci.*, *55*, 3264–3282.

Grant, K. E., C. C. Chuang, A. S. Grossman, and J. E. Penner (1999), Modeling the spectral optical properties of ammonium sulfate and biomass burning aerosols: Parameterization of relative humidity effects and model results, *Atmos. Environ.*, *33*, 2603–2620.

Guo, H., J. E. Penner, M. Herzog, and X. Liu (2004), Comparison of the vertical velocity used to calculate the cloud droplet number concentration in a cloud resolving and a global climate model, paper presented at the Fourteenth ARM Science Team Meeting Proceeding, Atmospheric Radiation Measurement (ARM) Program, Albuquerque, New Mexico, 22–26 March.

Guo, H., J. E. Penner, and M. Herzog (2005), Investigation of the impact of aerosols on clouds during the May 2003 Intensive Operational Period at the Southern Great Plains, paper presented at the Fifteenth ARM Science Team Meeting, Atmospheric Radiation Measurement (ARM) Program, Daytona Beach, Florida, 14–18 March.

Guo, H., J. E. Penner, M. Herzog, and H. Pawlowska (2007), Examination of the aerosol indirect effect under contrasting environments during the ACE-2 experiment, *Atmos. Chem. Phys.*, *7*, 535–548.

Han, Q., W. Rossow, and A. A. Lacis (1994), Near-global survey of effective droplet radii in liquid water clouds using ISCCP data, *J. Clim.*, *7*, 465–497.

Han, Q., W. Rossow, J. Zeng, and R. Welch (2002), Three different behaviors of liquid water path of water clouds in aerosol-cloud interactions, *J. Atmos. Sci.*, *59*, 726–735.

Haywood, J., and O. Boucher (2000), Estimates of the direct and indirect radiative forcing due to tropospheric aerosols: A review, *Rev. Geophys.*, *38*, 513–543.

Herzog, M., H. Graf, C. Textor, and J. M. Oberhuber (1998), The effect of phase changes of water on the development of volcanic plumes, *J. Volcanol. Geotherm. Res.*, *87*, 55–74.

Herzog, M., J. M. Oberhuber, and H. F. Graf (2003), A prognostic turbulence scheme for the non-hydrostatic plume model, *J. Atmos. Sci.*, *60*, 2783–2796.

Jiang, H., and G. Feingold (2006), Effect of aerosol on warm convective clouds: Aerosol-cloud-surface flux feedbacks in a new coupled large eddy model, *J. Geophys. Res.*, *111*, D01202, doi:10.1029/2005JD006138.

Jiang, H., G. Feingold, and W. R. Cotton (2002), Simulations of aerosol-cloud-dynamical feedbacks resulting from entrainment of aerosol into the marine boundary layer during the Atlantic Stratocumulus Transition Experiment, *J. Geophys. Res.*, *107*(D24), 4813, doi:10.1029/2001JD001502.

Kessler, E. (1969), On the distribution and continuity of water substance in atmospheric circulation, *Meteorol. Monogr.*, *10*, 84 pp.

Liu, Y., and P. Daum (2004), Parameterization of the autoconversion process. part I: Analytical formulation of the Kessler-type parameterization, *J. Atmos. Sci.*, *61*, 1539–1548.

Lohmann, U., and J. Feichter (2005), Global indirect aerosol effects: A review, *Atmos. Chem. Phys.*, *5*, 715–737.

Lohmann, U., J. Feichter, C. C. Chuang, and J. E. Penner (1999), Prediction of the number of cloud droplets in the ECHAM GCM, *J. Geophys. Res.*, *104*, 9169–9198.

Lu, M.-L., and J. H. Seinfeld (2005), Study of the aerosol indirect effect by large-eddy simulation of marine stratocumulus, *J. Atmos. Sci.*, *62*, 3909–3932.

Martin, G. M., D. W. Johnson, and A. Spice (1994), The measurement and parameterization of effective radius of droplets in warm stratocumulus clouds, *J. Atmos. Sci.*, *51*, 1823–1842.

Medeiros, B., A. Hall, and B. Stevens (2005), What controls the mean depth of the PBL?, *J. Atmos. Sci.*, *62*, 3157–3172.

Min, Q.-L., and L. C. Harrison (1996), Cloud properties derived from surface MFRSR measurements and comparison with GOES results at the ARM SGP site, *Geophys. Res. Lett.*, *23*(13), 1641–1644.

Min, Q.-L., L. C. Harrison, and E. E. Clothiaux (2001), Joint statistics of photon path length and cloud optical depth: Case studies, *J. Geophys. Res.*, *106*(D7), 7375–7385.

Min, Q.-L., M. Duan, and R. Marchand (2003), Validation of surface retrieved cloud optical properties with in-situ measurements at the Atmospheric Radiation Measurement Program (ARM) South Great Plains site, *J. Geophys. Res.*, *108*(D17), 4547, doi:10.1029/2003JD003385.

Moeng, C.-H., et al. (1996), Simulation of a stratocumulus-topped planetary boundary layer: Intercomparison among different numerical codes, *Bull. Amer. Meteor. Soc.*, *77*, 261–278.

Moeng, C.-H., J. C. McWilliams, P. Rotunno, P. P. Sullivan, and J. Weil (2004), Investigating 2D modeling of atmospheric convection in the PBL, *J. Atmos. Sci.*, *61*, 889–903.

Oberhuber, J., M. Herzog, H. Graf, and K. Schwanke (1998), Volcanic plume simulation on large scales, *J. Volcanol. Geotherm. Res.*, *87*, 29–53.

Penner, J. E., et al. (2001), Report to Intergovernmental Panel on Climate Change from the Scientific Assessment Working Group (WGI), in *Climatic Change 2001: The Scientific Basis*, chap. 5, edited by J. T. Houghton et al., pp. 289–348, Cambridge Univ. Press, New York.

Penner, J. E., X. Dong, and Y. Chen (2004), Observational evidence of a change in radiative forcing due to the indirect aerosol effect, *Nature*, *427*(15), 231–234.

Stevens, B., W. R. Cotton, and G. Feingold (1998), A critique of one- and two-dimensional models of boundary layer clouds with a binned representations of drop microphysics, *Atmos. Res.*, *47–48*, 529–553.

Stevens, B., et al. (2001), Simulations of trade wind cumuli under a strong inversion, *J. Atmos. Sci.*, *58*, 1870–1891.

Stull, R. B. (1988), *An Introduction to Boundary Layer Meteorology*, Kluwer Aacad. Publ., Netherlands.

Textor, C., H.-F. Graf, M. Herzog, and J. M. Oberhuber (2003), Injection of gases into the stratosphere by explosive volcanic eruptions, *J. Geophys. Res.*, *108*(D19), 4606, doi:10.1029/2002JD002987.

Twomey, S. (1977), The influence of pollution on the shortwave albedo of clouds, *J. Atmos. Sci.*, *34*, 1149–1152.

Xie, S., R. T. Cederwall, and M. Zhang (2004), Developing long-term single-column model/cloud system-resolving model forcing data using numerical weather prediction products constrained by surface and top of the atmosphere observation, *J. Geophys. Res.*, *109*, D01104, doi:10.1029/2003JD004045.

Zhang, M. H., and J. L. Lin (1997), Constrained variational analysis of sounding data based on column-integrated budgets of mass, heat, moisture, and momentum: Approach and application to ARM measurements, *J. Atmos. Sci.*, *54*, 1503–1524.

_____

H. Guo and J. E. Penner, Department of Atmospheric, Oceanic and Space Sciences, 1546 Space Research Building, 2455 Hayward Street, Ann Arbor, MI 48109-2143, USA. (hguo@umich.edu)

M. Herzog, Geophysical Fluid Dynamics Laboratory, National Oceanic and Atmospheric Administration, Princeton, NJ 08542, USA.

S. Xie, Atmospheric Science Division, Lawrence Livermore National Laboratory, Livermore, CA 94550, USA.